# Design and Implementation of Surface Eroding Thermocouples for Stage One Modular Divertor Integration at the DIII-D Tokamak

J. Ren [a]*, T. Elsey [b], C. Murphy [b], B.Z. Zhao [a], M. Shafer [c], R. Wilcox [c], S. Hong [b], R. Hood [d], C. Tsui [d], D. Donovan [a]

[a] *University of Tennessee – Knoxville, Knoxville, USA*

[b] *General Atomics, San Diego, USA*

[c] *Oak Ridge National Laboratory, Oak Ridge, USA*

[d] *Sandia National Laboratories, Livermore, USA*

*Corresponding author: rjun@utk.edu

# Design and Implementation of Surface Eroding Thermocouples for Stage One Modular Divertor Integration

DIII-D has upgraded its upper divertor to a modular system using copper alloy pedestals to alter divertor geometry without changing the vessel structure. Six new graphite tiles were designed for the Shape and Volume Rise (SVR) divertor. These new SVR tiles facilitated the formation of a poloidal array of 27 Surface Eroding Thermocouples (SETCs) in the upper divertor region. At one location, a specialized recessed SETC, paired with a standard flush SETC, was installed in one of the ceiling tiles to provide comprehensive heat flux measurements, distinguishing between charged and non-charged particle contributions. Upgrades were made to the SETC system in the Small Angle Slot (SAS) divertor to improve overall performance. These upgrades include optimizing the feedthrough system to double thermocouple cable capacity and reallocating cables from the SAS area to the SVR divertor. A compact isolation amplifier system with a fixed gain of 41 was employed to improve the signal level and minimize interference. Additionally, two analog-to-analog fiber systems have been implemented for transmitting thermocouple signals over a single fiber, significantly reducing both noise levels and costs. The newly installed SETCs in the SVR divertor successfully completed initial commissioning testing. The SETCs captured the in-out asymmetry in power distribution between the inner and outer strike points and demonstrated the dependency of the heat flux profile on the outer strike point location. During divertor detachment, heat flux mitigation was noted at the outer strike point location, while significant heat flux contributions from neutral particles were measured in the SVR divertor.

Keywords: divertor, diagnostics, heat flux.

Subject classification codes: include these here if the journal requires them

## Introduction

As fusion research progresses towards the realization of sustainable fusion energy, the challenges presented by the plasma-wall interactions become increasingly critical [1]. The extreme conditions within fusion reactors, characterized by high temperatures and intense particle fluxes, necessitate advanced diagnostic techniques to accurately monitor heat fluxes to plasma facing components

(PFCs), especially in the divertor area where the plasma directly interacts with PFCs [2]. Moreover, effective heat flux management strategies are essential to prevent material degradation and ensure the longevity and efficiency of fusion devices [3].

In DIII-D, Surface Eroding Thermocouples (SETCs) have been developed specifically for the measurement of PFC surface temperature and local heat flux [4]. Throughout multiple consecutive experimental campaigns, SETCs have been successfully deployed in the small angle slot (SAS) divertor, establishing them as reliable and accurate instruments for heat flux assessment [5]. Utilizing the outstanding capability demonstrated by the SETCs, several topics were systematically investigated in DIII-D, including characterizing the heat flux profiles, identifying the divertor detachment and developing the feedback control [6, 7].

DIII-D has significantly enhanced its divertor system by upgrading from the previous upper divertor configuration to a novel modular divertor system. This innovative approach employs a series of copper alloy pedestals to enable substantial alterations in divertor geometry while leaving the vessel's water-cooled structures unchanged. To optimize plasma pedestal performance, the initial phase of this modular divertor initiative involves installing a shape and volume rise (SVR) divertor. This shape and volume manipulation aims at increasing plasma volume, upper triangularity and edge pressure. The new SVR divertor could increase the plasma volume by more than 5% and raise the triangularity to 0.9. Modelling further predicts that this shaping can enhance the pedestal pressure by ~30%, from 60 kPa to 80 kPa, thereby enabling a wider super-H mode access path and broadening the overall operational parameter range. [8]

As part of this project, integrating SETCs with the new SVR divertor was a critical task. To minimize the resources required for applying SETCs to the SVR divertor, we upgraded the current SETC system to meet the new requirements, thereby avoiding the need to construct an entirely new system. In this paper, we will present the design and advancements of the upgraded SETC system for the SVR divertor, along with preliminary physics results of characterizing the heat flux profile and heat flux mitigation during divertor detachment.

**Physical requirements of SVR divertor**

The upper divertor in the DIII-D facility has been optimized into a modular configuration to facilitate geometric modifications in a more rapid manner. The first phase of this upper divertor work involves implementing the Shape and Volume Rise (SVR) divertor to increase plasma volume and edge pressure, requiring careful consideration of heat flux measurements.

As shown in Figure 1, the upper divertor of DIII-D has been upgraded using a modular design to increase plasma volume. To achieve this, the old upper inner divertor, including the water-cooled structures and cryopump, was removed. Copper pedestals were installed on the ceiling by bolting their feet to the cooled vessel wall. New tiles were installed to the wall and the copper pedestal structure to create a plenum inboard of the outer divertor structure. This modification allows DIII-D to implement multiple divertor geometries at a lower cost and enhances the flexibility for incorporating diagnostic systems in the upper divertor. With the installation of newly designed tiles, the updated divertor geometry enables DIII-D to position the X-point closer to the divertor surface compared to the previous shape, resulting in increased plasma volume and higher upper triangularity, optimizing pedestal performance.

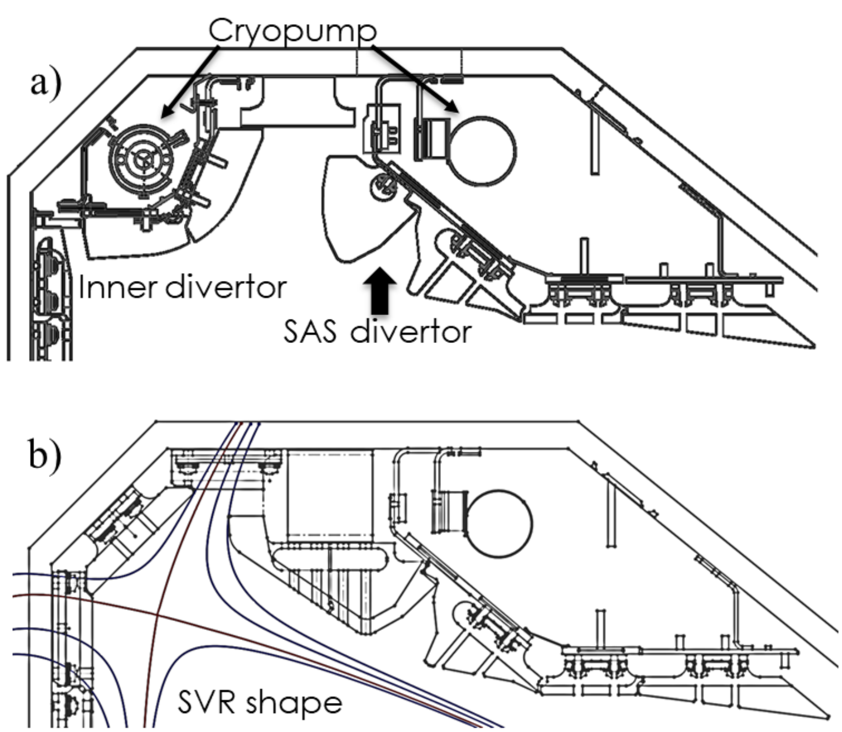

Figure. 1 Comparison of the DIII-D upper divertor system before (a) and after (b) the installation of the first-stage modular divertor

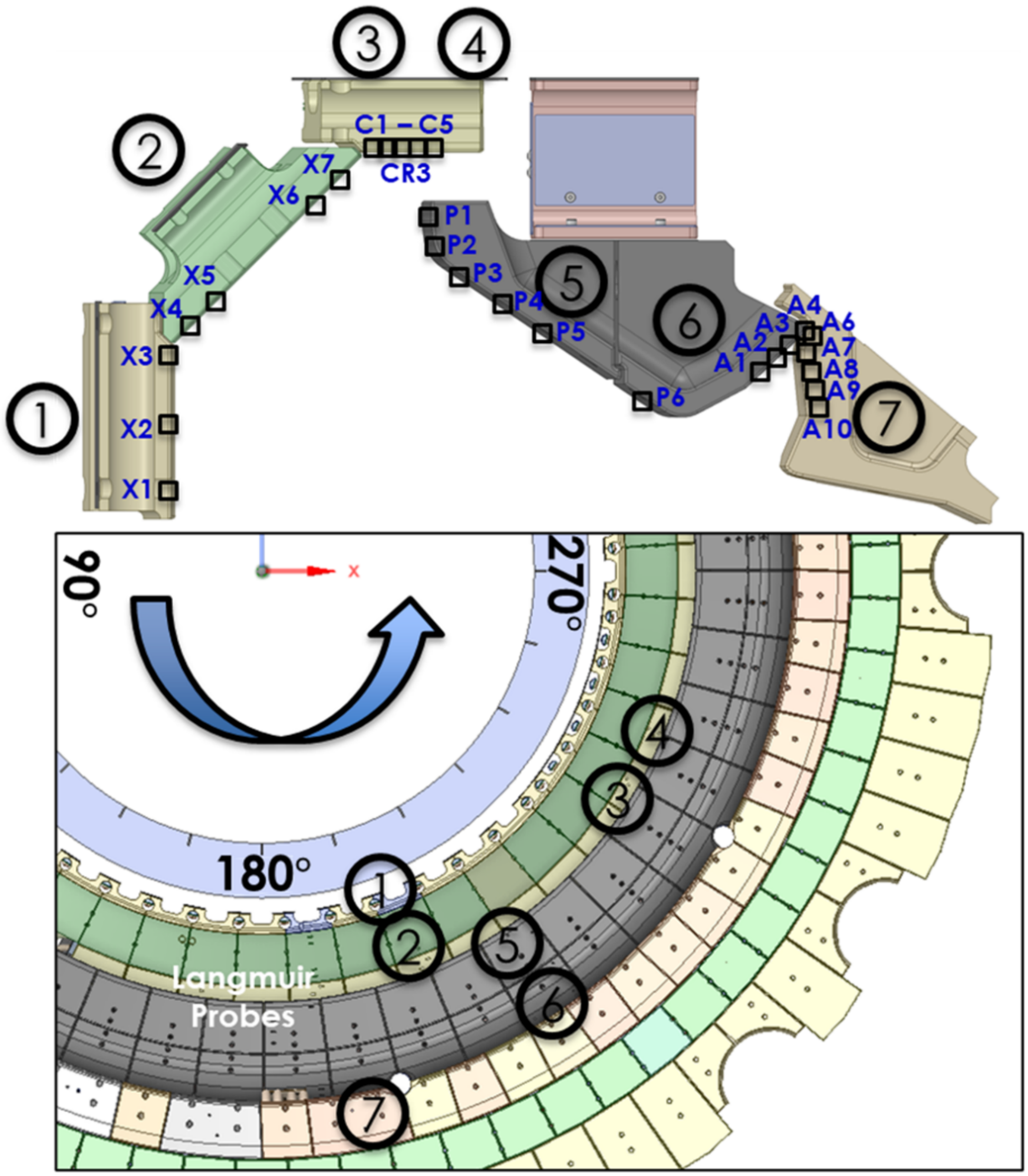


Figure. 2 poloidal and toroidal distributions of the seven SETC mounting tiles in the SVR divertor, with overlays and labels of the SETCs shown in the subplot. These tiles are identified as follows:1. Centerpost tile, 2. 45-degree tile, 3. Ceiling tile-1, 4. Ceiling tile-2, 5. Nose tile, 6. Inner SAS tile and 7. Outer SAS tile.

By positioning the X-point in close proximity to the divertor targets, the SVR configuration maximizes plasma volume but imposes significant constraints on the power dissipation area, leading to radiation peaks near the divertor target. Additionally, this shape broadens the poloidal flux expansion ($\boldsymbol{f_x}$) due to the shortened leg length [9]. The broadened poloidal flux expansion not only generates a wider power deposition band poloidally along the divertor surface but also results in a shallower field line angle at the divertor surface, as the local field line angle is inversely proportional to the flux expansion, expressed as $\boldsymbol{\theta}_{\perp} \propto \boldsymbol{f_x^{-1}}$ [10]. Consequently, heat flux measurements in the SVR divertor must cover not only the region near the separatrix but also the broader divertor surface to account for the heat flux deposited on various components. To meet these heat flux measurement requirements, six specialized tiles were designed and installed in the upper divertor to mount SETCs. The placement of these new SETCs was carefully considered to address the specific needs of heat flux measurement in the SVR divertor.

A total of 28 SETC units were integrated into seven (six new tiles, one existing tile) distinct tiles, forming a poloidal array within the upper divertor region of the DIII-D tokamak. In Figure 2, the shapes, relative locations and integration of seven divertor tiles in the upper divertor system from the centerpost to the outer SAS divertor are illustrated. These seven tiles overlap with the adjacent tile in the poloidal ordination. The duct beneath the nose tile is the entrance to the intermediate plenum for divertor density control. This intermediate volume connects to the main divertor plenum, where the cryopump is located behind the baffle. For the SVR configuration, the inner strike point (ISP) and the outer strike point (OSP) will basically locate at the centerpost tile and the ceiling tile respectively, as showing in the Figure 1 b). Due to engineering constraints, such as cooling pipes, magnetic coils, and puffing pipes beneath the tiles, the seven SETC mounting tiles are not located at the same toroidal position but are distributed between 192.5 and 247.5 degrees. The SETCs are toroidally positioned next to the Langmuir Probe diagnostics to minimize toroidal asymmetry and ensure accurate cross-calibration in heat flux measurements between these diagnostics [11]. Some detailed information about the distinct SETC mounting tiles can be found in the table 1.

| *Label* | *Tile name* | *Toroidal location* | *SETCs installed* |
|---|---|---|---|
| *1* | Centerpost tile | 202.5 | 3 |
| *2* | 45-degree tile | 202.5 | 4 |
| *3* | Ceiling tile1 | 240 | 3 |
| *4* | Ceiling tile 2 | 247.5 | 2+1(recessed) |
| *5* | nose tile | 217.5 | 5 |
| *6* | Inner SAS tile | 217.5 | 5 |
| *7* | Outer SAS tile | 192.5 | 5 |

Table 1. Information about SETC mounting tiles in the SVR project

**Design of the SETC mounting tiles**

As discussed above, 28 SETC units were installed on seven distinct tiles in the upper divertor of the DIII-D. To ensure accurate measurement of the heat flux seen by the divertor target, the SETC sensors were directly grounded to the graphite tile to ensure the sheath condition on the SETC surface is same as the divertor target. The structure and components used to secure the SETC sensors to the graphite tiles are depicted in Figure 3. To minimize potential failure risks associated with a complex mounting structure, a simplified design was implemented, incorporating only two components: a graphite nut and a spring. The graphite nut, with a 1/2-20 thread, provides consistent linear force to press the SETC sensor against the divertor surface. A Nimonic 90 alloy spring applies reliable spring force to the SETC sensor, ensuring that the sensor surface remains flush with the divertor target even during heating and cooling cycles throughout the plasma discharges.

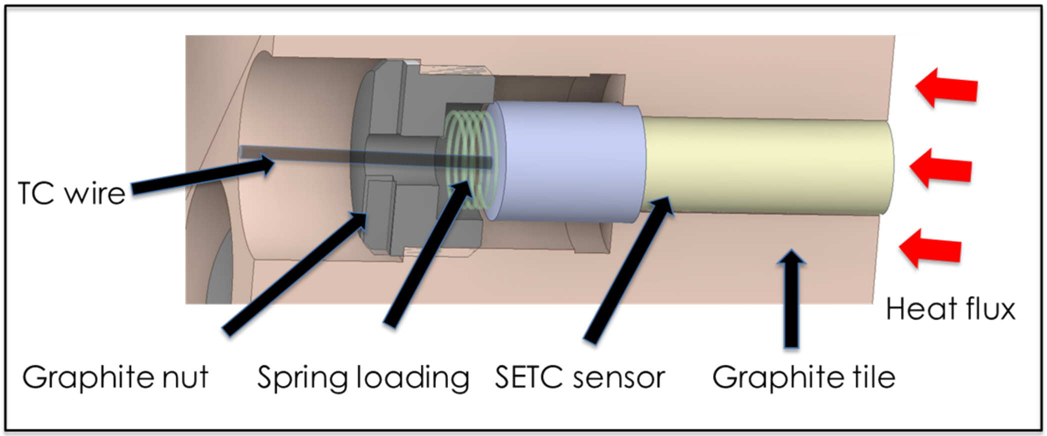


Figure 3. Cross-sectional diagram showing the mounting of a SETC sensor into a graphite tile

In DIII-D, power deposition on the divertor exhibits significant in-out asymmetry, with the majority of the power flowing along the separatrix to the outer divertor region, while less power reaches the inner strike point [12]. Consequently, more resources have been allocated to the OSP, including the placement of two SETC instrumented ceiling tiles to monitor the intense heat flux in this area.

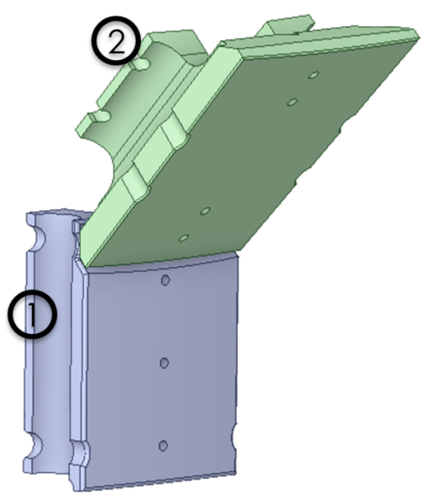


Figure 4. 3D drawing showing the design of the (1) Centerpost tile and the (2) 45-degree tile installed at the inner strike point location in the SVR divertor.

Figure 4 shows a 3D model detailing the geometry of two graphite tiles installed at the inner strike point location in the SVR divertor, with the positions of the SETC mounting hole on the plasma-facing surface. On the centerpost tile, where the inner strike point is typically located, three SETCs were installed equidistantly along the divertor surface, forming a reliable heat flux measurement array in the Scrape-Off Layer (SOL) region. In the 45-degree tile, the four SETCs were not equidistantly spaced; instead, they were paired up, with each pair installed near the top and bottom edges of the tile, respectively. Since the 45-degree tile is typically located in the Private Flux Region (PFR), this design allows the paired units to more effectively measure the heat flux that diffuses into the PFR from both the inner and outer SOL regions.

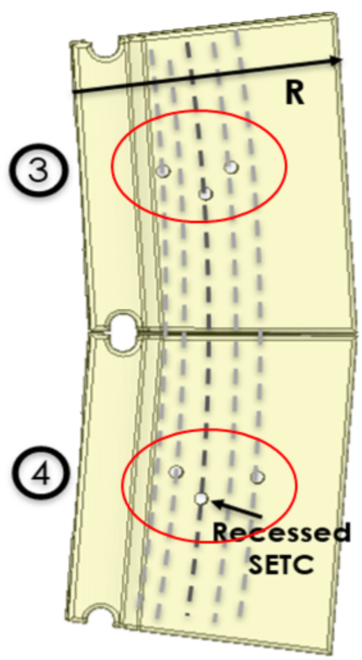


Figure 5. 3D drawing showing the design of the (3) Ceiling tile-1 and the (4) Ceiling tile-2 installed at the OSP location in the SVR divertor.

To measure the higher heat flux in the OSP area, six SETCs were installed in two graphite ceiling tiles, with three SETCs on each tile. Figure 5 shows the detailed design of the two ceiling tiles. Although the tiles have identical dimensions and geometry, the SETC distribution differs to meet the heat flux measurement requirements in the outer divertor leg region. Five of the SETCs were evenly spaced across five distinct physical locations along the major radius (R) direction, forming a dense heat flux measurement array at the OSP. Due to the fact that approximately half of the ceiling tile is positioned beneath the adjacent nose tile, as shown in Figure 2, no SETCs were installed in the remaining surface on the outboard side of the ceiling tiles, where the plasma flow is blocked. Additionally, a recessed SETC paired with a standard flush SETC was installed in the middle of the ceiling tile to provide comprehensive heat flux measurements, enabling the differentiation between charged and non-charged particle contributions. The detailed physical mechanism, as well as the methodology for using the combination of recessed and flush SETCs to quantify heat flux contributions from different sources, can be found in reference [13].

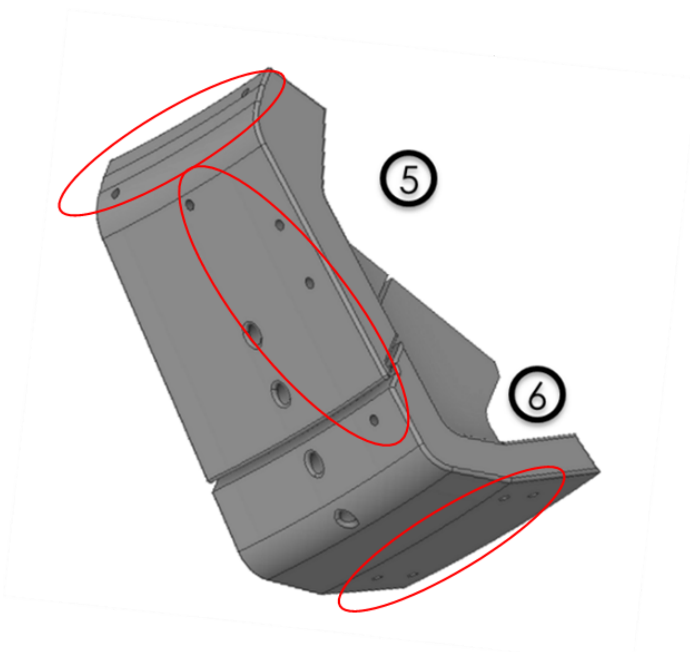

Figure 6. 3D drawing showing the design of the (5) SVR Nose tile and the (6) Inner SAS tile for the modular divertor integration

As discussed in the previous section, the SVR configuration requires the X-point to be positioned close to the divertor surface, which increases flux expansion at the divertor. As a result, the heat flux from the SOL is deposited over a relatively wide area at the divertor surface. Consequently, this necessitates heat flux measurements covering a larger area along the outer divertor surface. The compact divertor volume in the SVR configuration leads to radiation peaking in the outer divertor region, directing considerable radiative power onto nearby surfaces. To monitor the heat flux from the far SOL and the radiative power, which are crucial for understanding divertor heat loads and ensuring machine safety, five SETCs were installed on the vertical and gradually sloped surfaces of the SVR Nose tile, as shown in Figure 6.

**Adaption of the SAS divertor to meet new requirements**

Before the implementation of the modular divertor in DIII-D, SETCs were already installed in the SAS divertor, a system designed to achieve divertor detachment at lower plasma densities—a milestone for DIII-D, completed in FY23 [14-17]. In order to minimize the resource required to apply SETCs to SVR divertor, we modified the current SETC system in the SAS divertor to meet the new SVR requirements.

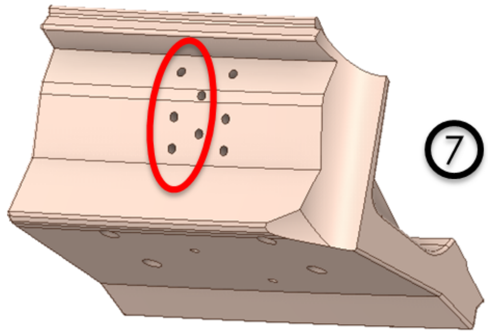


Figure 7. 3D drawing of the outer inner SAS tile for modular divertor integration, with the remaining SETCs highlighted in red circle

Due to changes in the geometry and mounting structure of the Inner SAS tile, a new tile was designed to replace the old SAS tile. In the new Inner SAS tile, the target surface inside the SAS slot retains the same as the previous SAS divertor, allowing for the repetition of SAS divertor-related experiments with the identical divertor closure. The number of SETCs installed on the new Inner SAS tile remains the same as in the previous SAS divertor, but one SETC has been relocated from near the vertex to outside the SAS slot due to engineering constraints in the new tile design (see Figure 6). The Outer SAS tile in the modular divertor remains unchanged from the previous SAS campaign, but five SETCs were removed from it to accommodate additional SETCs in the more critical SVR divertor areas. The remaining five SETCs in the outer SAS tile for modular divertor integration are highlighted inside red circle in Figure 7.

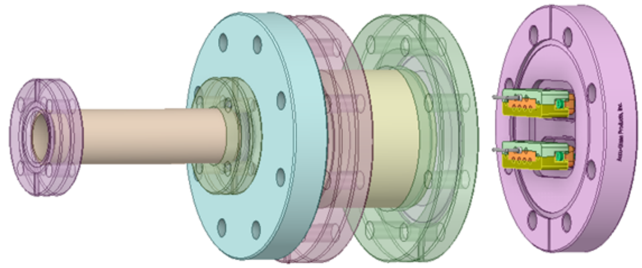


Figure 8. Schematic diagram of the upgraded feedthrough port designed for supporting the SETCs to the SVR modular divertor in DIII-D

In DIII-D, high-purity magnesium oxide (MgO) mineral-insulated thermocouple cables were selected for in-vacuum SETC applications due to their optimal combination of space efficiency, durability in the harsh tokamak environment, electromagnetic compatibility, and ease of implementation. As shown in Figure 8, to increase the thermocouple cable capacity within the constraints of the limited feedthrough port, feedthrough fittings were employed to adapt a 2-1/8" CF flange to 4-1/2" CF double sub-D connector feedthroughs. By utilizing a specifically designed PEEK connector for the 7-pair thermocouple cables, the capacity of each feedthrough was effectively doubled compared to the single sub-D connector feedthroughs previously utilized in the SAS campaign. The total available 28 pairs of thermocouple wires were also reallocated to prioritize the requirements for the SETCs installed in the SVR divertor. As a result, 18 SETCs were placed in the SVR divertor to investigate the divertor physics in high-volume plasma conditions, while 10 SETCs remained in the SAS divertor to ensure baseline heat flux measurement capability for SAS divertor operation.

**Enhancements in signal processing and transmission**

The SETCs used in DIII-D employ standard Type C junctions made from tungsten-rhenium alloys, capable of withstanding extreme temperatures up to 2320°C. However, these junctions generate only ~0.018 mV/°C of thermoelectric voltage below 1000°C, which is marginal for precise measurements in the tokamak environment. As the SETC sensors are grounded directly to the machine wall, it is crucial to ensure that each measurement channel is electrically isolated to prevent the machine potential from escaping and to minimize channel-to-channel interference. A 32-channel isolation amplifier system was designed and implemented to isolate and enhance the thermocouple signals. This system utilizes 32 AMC1302 reinforced isolated amplifiers, each with a fixed gain of 41, low error, and minimal drift. The amplifiers feature ±50 mV input and provide 5000 VRMS isolation. This gain was chosen to maximize the thermal voltage signal while ensuring it remains safely below the fiber link voltage limit with sufficient margin.

To transmit the thermocouple signals from the DIII-D hall to the digitizer, fiber optic links were utilized. In the modular divertor project, the AFL-6416 enhanced fiber optic transmission system was introduced, replacing the conventional one-to-one optical fiber setup. This new advanced system can simultaneously transmit 16 analog signals at a 198 kHz sampling rate and with a 25 kHz bandwidth per signal, all over a single optical fiber with 16-bit accuracy. The implementation of this new fiber optic system significantly reduces the amount of fiber required, which decreases costs and minimizes the need for wall openings, thereby enhancing neutron protection. Additionally, it improves signal quality by eliminating electromagnetic interference (EMI) during transmission. Two AFL-6416 systems were installed to manage the 28 channels of SETCs in the modular divertor system. Figure 9 shows images of both the isolation amplifier system and the fiber optic transmission systems that have been established at DIII-D.

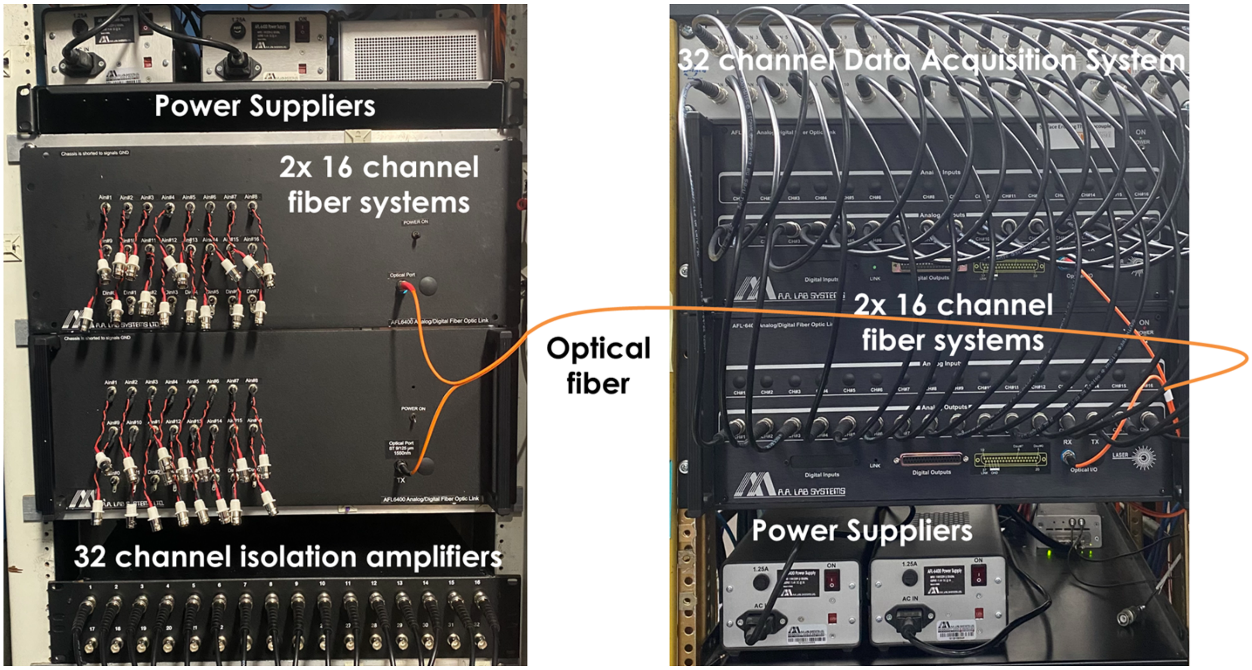


Figure 9. Photos of the isolation amplifier system and the fiber optic transmission systems installed at DIII-D.

**Commissioning of SETC in the modular divertor system**

The first measurement from the SETC in the modular divertor system was achieved during the initial commissioning test. For a typical shot, 199087, conducted during this test, the plasma parameters were as follows: plasma current $Ip$=1.43 MA, toroidal magnetic field $B_T$=−2.20T, and auxiliary heating neutral beam power $P_{NBI}$=11MW. The test involved sweeping the strike point location, specifically shifting the OSP from $R$=1.16 m to $R$=1.26 m, transitioning from the ceiling tile to the nose tile, as illustrated by the two plasma equilibriums reconstructed by Equilibrium Fitting (EFIT) at 2.7 seconds and 4.4 second in Figure 10. It also shows the perpendicular heat flux measured by the SETCs installed in the modular divertor along the surface from the centerpost tile to the entrance of the SAS divertor. In the contour plot, the vertical axis represents the distance from the inner mid-plane, moving counter clockwise along the first wall surface. The locations of the inner and OSPs are highlighted with white and red dashed lines respectively.

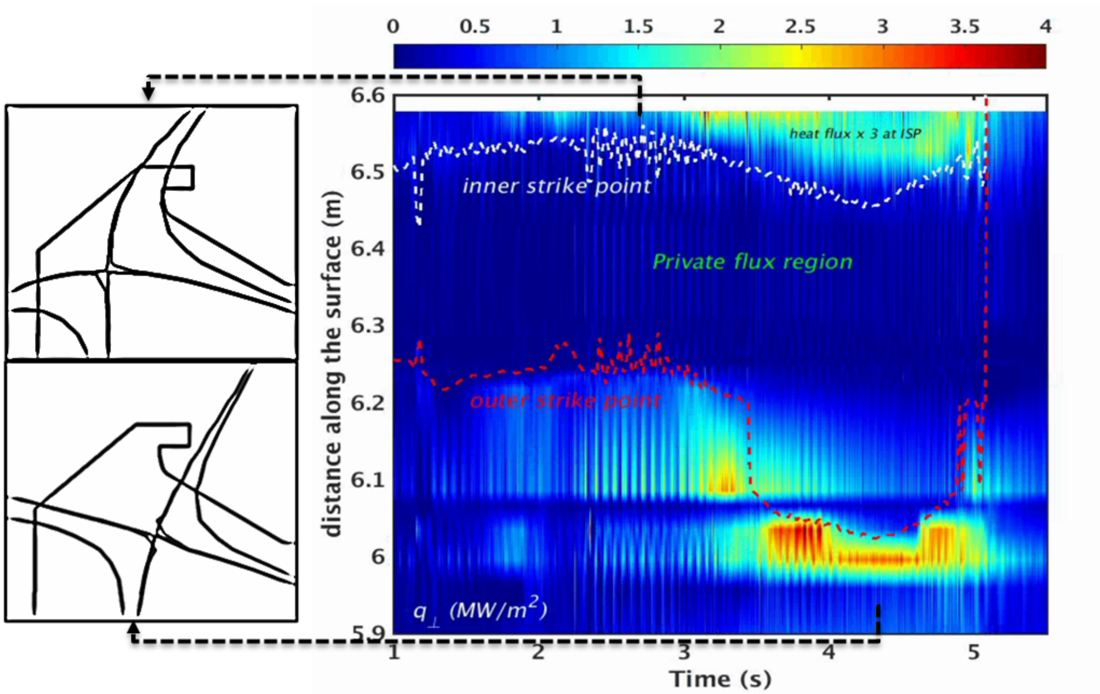


Figure 10. Contour plot of perpendicular heat flux measured by SETCs installed along the SVR divertor surface, along with two plasma equilibriums reconstructed by EFIT at the start and end of the strike point sweep

In this plasma discharge, as the strike point sweeps across the divertor, the heat flux measured by the SETCs varies, increasing and decreasing as the strike point moves closer to or further away from the measuring sensors at both the inner and outer divertor regions. The peak heat flux at the inner divertor is consistently located on the inboard side of the strike point, whereas at the outer divertor, the peak heat flux is on the outboard side of the strike point. This indicates that the peak heat fluxes are always situated at the SOL of both strike points. Note that the heat flux near the inner strike point has been multiplied by a factor of 3 for better comparison with the OSP heat flux, making it distinguishable in the contour plot. This confirms a significant in-out asymmetry in power distribution between the inner and OSPs. The maximum heat flux in the SVR divertor, measured at the OSP on the nose tile surface, is approximately 4 MW/m², while the PFR remains effectively cold throughout the discharge. A cold band at outer divertor is observed at the corner of the nose tile, likely due to the local shallow field line angle.

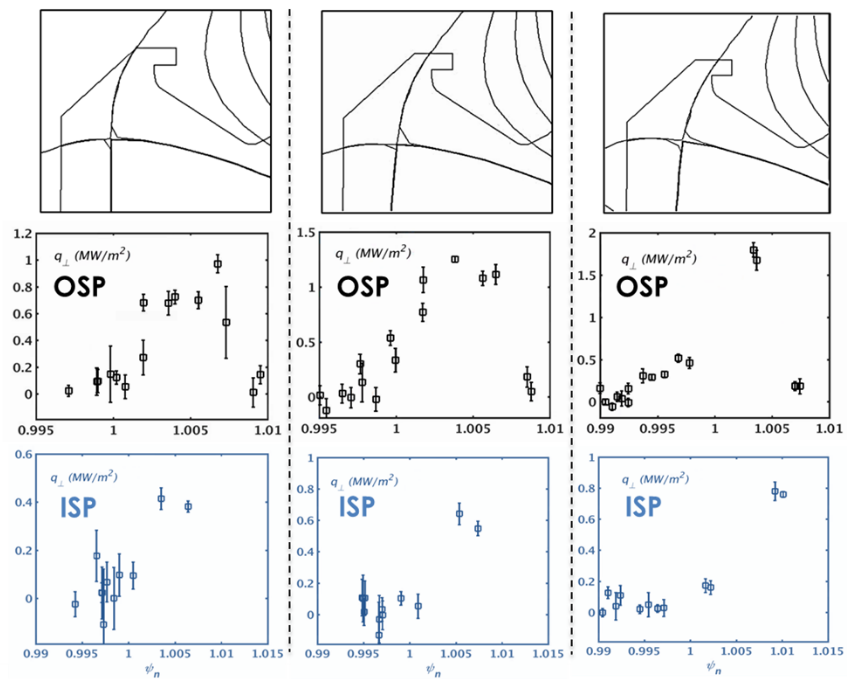


Figure 11. Heat flux profile measured by SETCs at the OSP (black) location and ISP location (blue), with OSPs positioned at different locations on the ceiling tile. The plasma equilibriums were reconstructed by EFIT.

To further characterize heat flux behavior in the modular divertor, three plasma shapes with OSPs positioned at different locations on the ceiling tile were selected. These configurations were chosen to explore the divertor heat flux profile while maximizing the plasma volume in the SVR divertor. As shown in Figure 11, the heat flux profiles measured at both the OSP location (in black) and the ISP location are displayed in the second and third rows, respectively. The SETC provides a reasonable heat flux profile at the OSP location. However, due to the limited number of SETC units installed at the ISP location, it can only capture the maximum heat flux at the ISP rather than a complete profile. In the plots, the heat flux is shown for three short intervals during an OSP location sweep. From left to right, the columns correspond to the OSP locations: the inner corner of the ceiling tile, the center of the ceiling tile, and the duct entrance on the ceiling tile. When the OSP is located at the inner corner of the ceiling tile, the heat flux at the OSP peaks at $\varphi_n \sim 1.006$ with a perpendicular heat flux of approximately 1 MW/m². At the ISP location, the maximum heat flux is around 0.4 MW/m², reflecting the previously mentioned in-out asymmetry in power deposition. As the OSP shifts to the center of the ceiling tile, the heat flux profile at the OSP flattens, and increase to a maximum of about 1.2 MW/m². This could be due to the separatrix moving closer to the pump duct, reducing the neutral density and thus lowering the cooling effect near the strike point. For this OSP position, the maximum heat flux at ISP location also increases to around 0.6 MW/m². When the OSP is positioned at the entrance of the pump duct, strong interaction occurs at the nose tile, where the heat flux peaks at ~1.7 MW/m². Additionally, it was observed that increased power diffuses into the PFR, as indicated by a significant 0.5 MW/m² measured by SETC at $\varphi_n \sim 0.998$. Under this condition, the maximum heat flux at the ISP reaches approximately 0.8 MW/m². In all three cases, the ratio between the maximum heat flux at the OSP and ISP remains about ~2.

The successful commissioning of the SETC in the SVR modular divertor demonstrates the effectiveness of this diagnostic tool in accurately measuring heat flux and characterizing the thermal behavior of the divertor.

**Divertor detachment and radiation**

Divertor detachment is recognized as one of the most promising solutions to reduce peak heat flux on the divertor surface. In the newly installed SVR divertor, which maximizes plasma volume, the dynamics and heat flux mitigation during divertor detachment were investigated.

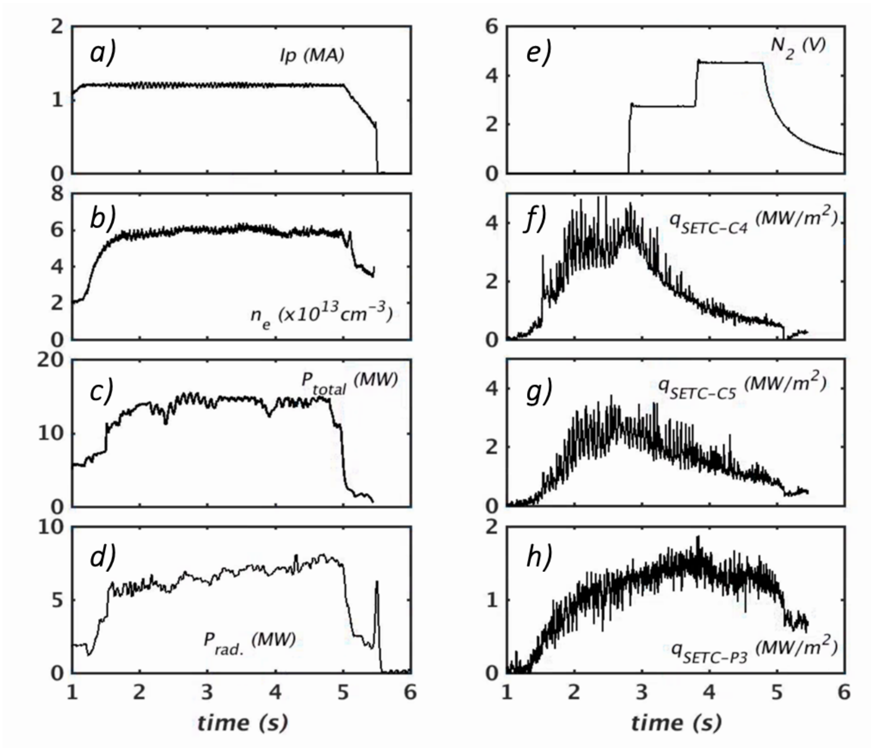


Figure 12. Evolution of plasma parameters and heat fluxes measured by SETCs during DIII-D discharge #201227. a) plasma current Ip, b) line average electron density ne, c) total inject power Ptotal, d) total radiation power Prad., e) nitrogen puffing N2, f) heat flux measured by SETC-C4 at near SOL $q_{SETC\text{-}C4}$, g) heat flux measured by SETC-C5 at near SOL $q_{SETC\text{-}C5}$ and h) heat flux measured by SETC-p3 at far SOL $q_{SETC\text{-}p3}$.

Figure 12 illustrates the evolution of key plasma parameters during the nitrogen-seeding induced divertor detachment plasma discharge #201227, which was conducted from the SVR divertor with the ion $B \times \nabla B$ drift direction was away from the divertor. In this upper single null discharge, the OSP was positioned at the middle of the ceiling tile with an elongation of $\kappa = 1.738$ and upper triangularity $\delta_{upper} = 0.954$. Nitrogen seeding was introduced by injecting $N_2$ through the PFX1 gas valve at the upper divertor location. During this discharge, the plasma current remained stable at $I_p$ = 1.2 MA, the plasma density was stable at $n_e = 6\times10^{13}$ cm$^{-3}$, and the total injected power was $P_{total}$ = 14.5 MW. At 2.8 s, $N_2$ puffing was initiated with a gas valve control voltage of 2.7 V, corresponding to an $N_2$ flow rate of 10.7 Torr·L/s. Simultaneously, the heat flux measured by SETC-C4 and SETC-C5 at the near SOL on the ceiling tile began to decrease, indicating the onset of detachment near the OSP location. As the $N_2$ puffing rate increased to 20.7 Torr·L/s (with a 4.5 V control voltage) at 3.8 s, the heat flux continued to decrease at the near SOL. The peak heat flux near the OSP dropped from approximately 3.5 MW/m² to about 0.7 MW/m² during detachment, representing an 80% reduction in heat flux. With continued $N_2$ injection, the total radiation power from the plasma gradually increased from approximately 6 MW to 7.5 MW. However, the heat flux at the far SOL, measured by SETC on the nose tile, did not decrease after the initial $N_2$ puffing. Only after the second increase in $N_2$ puffing did the heat flux at the far SOL begin to roll over. This indicates that, despite nitrogen seeding during this discharge, only partial detachment was achieved. Additional $N_2$ puffing is required to reach a full detachment divertor condition.

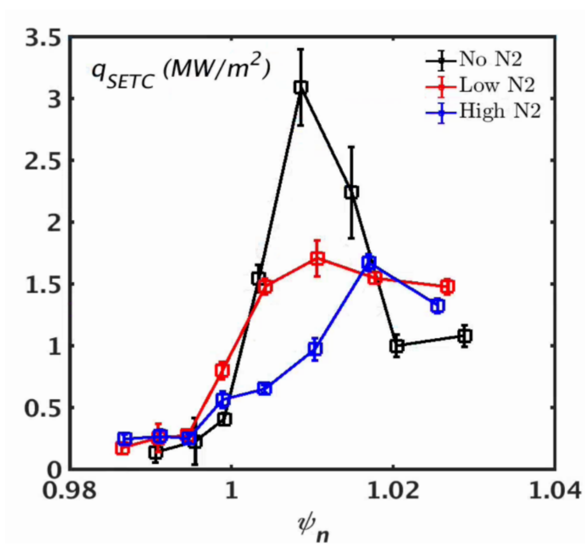


Figure 13. Comparison of heat flux profiles measured by SETC at the OSP location for cases with no nitrogen seeding, lower $N_2$ puffing rate, and higher $N_2$ puffing rate.

The dense SETC array installed at the SVR divertor successfully captured the evolution of the heat flux profile at the OSP location during the nitrogen seeding process. As shown in Figure 13, the heat flux profiles measured by SETC before $N_2$ puffing, during the lower $N_2$ flow rate, and at higher flow rates are illustrated as a function of the normalized poloidal flux ($\psi_n$). It is evident that, before the $N_2$ gas puffing into the SVR divertor, the heat flux at the OSP exhibits a sharp peak at $\psi_n$= 1.01, with a magnitude exceeding 3 MW/m². With the lower $N_2$ puffing rate, the maximum heat flux significantly decreases by approximately 50%, and the heat flux profile becomes flatter. However, the far SOL heat flux at $\psi_n$= 1.03 even slightly increases. This is likely due to the combination of the broadening of the heat flux profile associated with the onset of divertor detachment and the increased divertor radiation. With the higher $N_2$ puffing rate, the heat flux at $\psi_n$ = 1.01 further decreases to below 1 MW/m², indicating cold plasma conditions near the strike point location. In contrast, the heat flux at the far SOL remains high, suggesting that additional impurity seeding is required at the less closed nose tile to achieve a dissipative divertor condition.

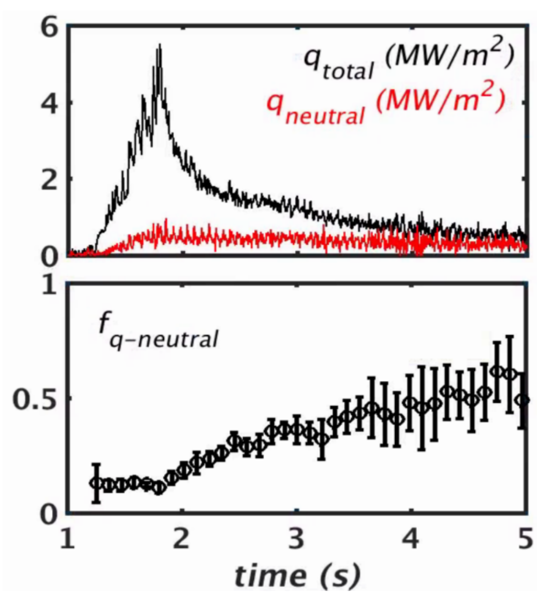

Figure 14. Evolution of total heat flux ($q_{total}$), heat flux from neutral particles ($q_{neutral}$) and fraction of heat flux from neutral particles ($f_{q-neutral}$)

As previously discussed, the close proximity of the X-point to the divertor surface in the SVR configuration imposes significant constraints on the dispersion area, potentially resulting in substantial radiative heat flux on the divertor surface. This study also examines the contribution of radiative photons to the surface heat flux in the SVR divertor during the detachment discharge. The flush SETC directly receives heat from charged particles along magnetic field lines, while the recessed SETC minimizes this contribution by reducing line-of-sight exposure. By implementing a combination of recessed and flush SETCs at the center of the ceiling tile, it becomes possible to separately measure the total deposited heat flux and the heat flux carried by neutral particles, including radiative photons and charge-exchange neutrals. In Figure 14, the total heat flux ($q_{total}$) measured by the flush-mounted SETC and the heat flux carried by neutral particles ($q_{neutral}$) measured by the recessed SETC are shown in red and black lines, respectively. During plasma discharge #201227, the OSP exhibited a slight outward drift prior to the initial nitrogen puffing, which gradually shifted the SETCs at the center of the ceiling tile into the PFR. Consequently, the sharp decline in total heat flux ($q_{total}$) before 2.8 seconds was due to the OSP movement, while the continued decrease afterward was attributed to divertor detachment. Although $q_{total}$ showed a continuous decline, the neutral heat flux ($q_{neutral}$) remained stable throughout the discharge, suggesting that the reduction in heat flux was primarily due to decreased contributions from ions and electrons. The stability of $q_{neutral}$ further indicates that radiative power and charge-exchange neutrals tend to be deposited uniformly over a large divertor area, showing low sensitivity to the OSP location. As detachment progressed, the fraction of heat flux from neutral particles rose dramatically from 10% to over 60%, suggesting that surface heating of the divertor during detachment was largely contributed by radiation and charge-exchange neutrals.

**Summary**

The successful upgrade of the DIII-D upper divertor system to a modular configuration, featuring the new SVR divertor, marks a significant advancement in DIII-D diagnostics and heat management. The integration of SETCs into this upgraded system has been executed with meticulous attention to both design and functionality, ensuring precise measurement of heat flux and effective differentiation between charged and non-charged particle contributions. Key enhancements to the SETC system, including increased thermocouple cable capacity, advanced signal amplification and isolation, and noise reduction through fiber optic links, have optimized the diagnostic capabilities of the modular divertor. Initial testing results confirm the good performance of the SETC system, providing reliable and accurate heat flux measurements. Preliminary results obtained from SETC measurements show that the SETCs captured the in-out asymmetry in power distribution between the inner and outer strike points and demonstrated the dependence of the heat flux profile on the outer strike point location. During divertor detachment, heat flux mitigation was observed at the outer strike point, while heat flux contributions from neutral particles significantly increased to 60% in the SVR divertor. The ongoing operation of these upgraded SETCs will yield valuable data over the FY24 to FY25, enhancing the understanding of plasma-wall interactions and divertor physics, while supporting the development of robust heat management strategies for future fusion reactors. This work not only demonstrates the effectiveness of the new divertor design but also highlights the critical role of continuous innovation in diagnostic technologies to address the challenges of sustainable fusion energy.

**Acknowledgment**

This material is based upon work supported by the U.S. Department of Energy, Office of Science, Office of Fusion Energy Sciences, using the DIII-D National Fusion Facility, a DOE Office of Science user facility, under Award(s) DE-FC02-04ER54698, DE-SC0019256 and DE-AC05-00OR22725, DE-NA0003525. **Disclaimer:** This report was prepared as an account of work sponsored by an agency of the United States Government. Neither the United States Government nor any agency thereof, nor any of their employees, makes any warranty, express or implied, or assumes any legal liability or responsibility for the accuracy, completeness, or usefulness of any information, apparatus, product, or process disclosed, or represents that its use would not infringe privately owned rights. Reference herein to any specific commercial product, process, or service by trade name, trademark, manufacturer, or otherwise does not necessarily constitute or imply its endorsement, recommendation, or favoring by the United States Government or any agency thereof. The views and opinions of authors expressed herein do not necessarily state or reflect those of the United States Government or any agency thereof.

**Reference**

[1] Kuang AQ, Ballinger S, Brunner D, et al, "Divertor heat flux challenge and mitigation in SPARC*," Journal of Plasma Physics,*86(5):865860505, 2020, doi：10.1017/S0022377820001117

[2] G. Janeschitz, "Plasma–wall interaction issues in ITER," *J Nucl Mater,* vol. 290-293, pp. 1-11, 2001/03/01/ 2001, doi: https://doi.org/10.1016/S0022-3115(00)00623-1.

[3] Y. Anquetin, J. Gaspar, Y. Corre, Q. Tichit, J. L. Gardarein, G. Laffont, M. Missirlian, and C. Pocheau, "Surface heat flux estimation with embedded thermocouples and Fiber Bragg Grating sensor in ITER-like plasma facing components," *Fusion Eng Des,* vol. 190, p. 113480, 2023/05/01/ 2023, doi: https://doi.org/10.1016/j.fusengdes.2023.113480.

[4] E. Kolemen, S. L. Allen, B. D. Bray, M. E. Fenstermacher, D. A. Humphreys, A. W. Hyatt, C. J. Lasnier, A. W. Leonard, M. A. Makowski, A. G. McLean, R. Maingi, R. Nazikian, T. W. Petrie, V. A. Soukhanovskii, and E. A. Unterberg, "Heat flux management via advanced magnetic divertor configurations and divertor detachment," *J Nucl Mater,* vol. 463, pp. 1186-1190, 2015/08/01/ 2015, doi: https://doi.org/10.1016/j.jnucmat.2014.11.099.

[5] J. Ren, D. Donovan, J. Watkins, H. Q. Wang, D. Rudakov, C. Murphy, A. McLean, C. Lasnier, E. Unterberg, D. Thomas, and R. Boivin, "The surface eroding thermocouple for fast heat flux measurement in DIII-D," *Rev Sci Instrum,* vol. 89, no. 10, p. 10J122, 2018, doi: 10.1063/1.5038677.

[6] J. Ren, D. Donovan, J. G. Watkins, H. Q. Wang, D. Rudakov, C. Murphy, E. Unterberg, D. Thomas, and R. Boivin, "Development of Surface Eroding Thermocouples in Small Angle Slot Divertor in DIII-D," *Ieee T Plasma Sci,* vol. 48, no. 6, pp. 1804-1809, 2020, doi: 10.1109/TPS.2019.2943085.

[7] J. Ren, D. C. Donovan, J. G. Watkins, H. Q. Wang, D. M. Thomas, and R. Boivin, "Experimental observation of heat flux mitigation during divertor detachment in the DIII-D small angle slot divertor," *Nuclear Materials and Energy,* vol. 26, p. 100887, 2021/03/01/ 2021, doi: https://doi.org/10.1016/j.nme.2020.100887.

[8] Buttery, R.J., Covele, B., Ferron, J. et al, "DIII-D Research to Prepare for Steady State Advanced Tokamak Power Plants," *J Fusion Energ* vol. 38, 72–111, 2019, https://doi.org/10.1007/s10894-018-0185-y.

[9] L. Casali, D. Eldon, A. McLean, T. Osborne, A. Leonard, B. Grierson, and J. Ren, "Impurity leakage and radiative cooling in the first nitrogen and neon seeding study in the closed DIII-D SAS configuration," *Nucl. Fusion,* vol. 62, no. 2, p. 026021, 2022/01/04 2022, doi: 10.1088/1741-4326/ac3e84.

[10] H. Anand, D. Humphreys, D. Eldon, A. Leonard, A. Hyatt, B. Sammuli, and A. Welander, "Plasma flux expansion control on the DIII-D tokamak," *Plasma Phys. Control. Fusion,* vol. 63, no. 1, p. 015006, 2020/11/13 2021, doi: 10.1088/1361-6587/abc457.

[11] A. U. t. the, T. Lunt, M. Bernert, D. Brida, P. David, M. Faitsch, O. Pan, D. Stieglitz, U. Stroth, and A. Redl, "Compact Radiative Divertor Experiments at ASDEX Upgrade and Their Consequences for a Reactor," *Phys Rev Lett,* vol. 130, no. 14, p. 145102, 04/04/ 2023, doi: 10.1103/PhysRevLett.130.145102.

[12] J. G. Watkins, H. Q. Wang, D. Thomas, C. Murphy, D. Taussig, J. Ren, C. Chrobak, and H. Y. Guo, "Langmuir probe array for the small angle slot divertor in DIII-D," *Rev Sci Instrum,* vol. 92, no. 5, p. 053523, 2021, doi: 10.1063/5.0043870.

[13] C. J. Lasnier, M. A. Makowski, J. A. Boedo, S. L. Allen, N. H. Brooks, D. N. Hill, A. W. Leonard, J. G. Watkins, and W. P. West, "Scaling of divertor heat flux profile widths in DIII-D," *J Nucl Mater,* vol. 415, no. 1, Supplement, pp. S353-S356, 2011/08/01/ 2011, doi: https://doi.org/10.1016/j.jnucmat.2010.12.008.

[14] J. Ren, D. C. Donovan, J. G. Watkins, H. Q. Wang, C. Lasnier, T. Looby, J. Canik, D. Rudakov, P. C. Stangeby, D. Thomas, and R. Boivin, "Measurements of multiple heat flux components at the divertor target by using surface eroding thermocouples (invited)," *Rev Sci Instrum,* vol. 93, no. 10, p. 103541, 2022/10/01 2022, doi: 10.1063/5.0101719.

[15] H. Y. Guo, H. Q. Wang, J. G. Watkins, L. Casali, B. Covele, A. L. Moser, T. Osborne, C. M. Samuell, M. W. Shafer, P. C. Stangeby, D. M. Thomas, J. Boedo, R. J. Buttery, R. Groebner, D. N. Hill, L. Holland, A. W. Hyatt, A. E. Jaervinen, A. Kellman, L. L. Lao, C. J. Lasnier, A. W. Leonard, C. Murphy, J. Ren, C. F. Sang, A. C. Sontag, and T. S. Taylor, "First experimental tests of a new small angle slot divertor on DIII-D," *Nucl. Fusion,* vol. 59, no. 8, p. 086054, 2019/07/09 2019, doi: 10.1088/1741-4326/ab26ee.

[16] T. Abrams, G. Sinclair, J. H. Nichols, E. A. Unterberg, D. C. Donovan, J. Duran, J. D. Elder, F. Glass, B. A. Grierson, H. Y. Guo, T. Hall, X. Ma, R. Maurizio, A. G. McLean, C. Murphy, R. Nguyen, D. L. Rudakov, P. C. Stangeby, D. M. Thomas, and S. A.

Zamperini, "Design and physics basis for the upcoming DIII-D SAS-VW campaign to quantify tungsten leakage and transport in a new slot divertor geometry," *Phys Scripta,* vol. 96, no. 12, p. 124073, 2021/12/01 2021, doi: 10.1088/1402-4896/ac3c5f.
[17] X. Ma, H. Q. Wang, H. Y. Guo, P. C. Stangeby, E. T. Meier, M. W. Shafer, and D. M. Thomas, "First evidence of dominant influence of E × B drifts on plasma cooling in an advanced slot divertor for tokamak power exhaust," *Nucl. Fusion,* vol. 61, no. 5, p. 054002, 2021/04/12 2021, doi: 10.1088/1741-4326/abde75.
[18] R. Maurizio, D. Thomas, J. H. Yu, T. Abrams, A. W. Hyatt, J. Herfindal, A. Leonard, X. Ma, A. G. McLean, J. Ren, F. Scotti, M. W. Shafer, G. Sinclair, H. Q. Wang, and J. Watkins, "Experiments on plasma detachment in a V-shaped slot divertor in the DIII-D tokamak," *Nucl. Fusion,* vol. 64, no. 8, p. 086048, 2024/07/03 2024, doi: 10.1088/1741-4326/ad58f4.